Electric-Field-Induced Solid−Gas Interfacial Chemical Reaction in Carbon Nanotube Ensembles: Route toward Ultra-sensitive Gas Detectors

Itisha Dwivedi, Arup Sarkar, Gopalan Rajaraman,* and Chandramouli Subramaniam*

Cite This: *ACS Appl. Mater. Interfaces* 2022, 14, 13271−13279

Read Online

ACCESS | Metrics & More | Article Recommendations | SI Supporting Information

ABSTRACT: The electric field at the sharp pointed tips of single wall carbon nanotube ensembles has been utilized to kinetically accelerate hitherto unobserved chemical reactions at the heterogeneous solid−gas interfaces. The principle of "action-of-points" drives specific chemical reactions between the defect sites of single wall carbon nanotubes (CNTs) and ppb levels of gaseous hydrogen sulfide. This is manifested as changes in the electrical conductivity of the conductive CNT-ensemble (cCNT) and visually tracked as enthalpic modulations at the site of the reaction through infrared thermometry. Importantly, the principle has been observed for a variety of analytes such as NH_3, H_2O, and H_2S, leading to distinctly correlatable changes in reactivity and conductivity changes. Theoretical calculations based on the density functional theory in the presence and absence of applied electric field reveal that the applied electric field activates the H_2S gas molecules by charge polarization, yielding favorable energetics. These results imply the possibility of carrying out site-specific chemical modifications for nanomaterials and also provide transformative opportunities for the development of miniaturized e-nose-based gas analyzers.

KEYWORDS: *electric field at heterogeneous solid−gas interface, carbon-based nanomaterials, gas analyzers, density functional calculations, site-specific unconventional reactions*
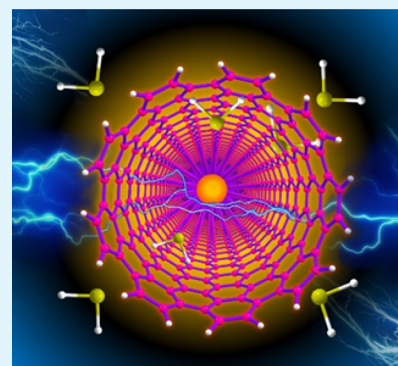
INTRODUCTION

Thermal activation has been a predominant route for carrying out several reactions of global importance such as the production of NH_3,[1−5] petroleum refining, and CO oxidation.[6−8] Although temperature has been a predominant driving force for these reactions, the means to achieve and sustain such high temperatures are constantly evolving toward newer approaches. In this direction, mechanochemical routes for driving chemical reactions have lowered the energy demand and simultaneously produced unconventional products.[9] Similarly, microwave-triggered reactions depend on the activation of specific chemical bonds with localized temperatures in excess of 1273 K.[10] However, the use of the electric field to drive reactions at the heterogeneous solid−gas interface has been sparingly explored thus far. Electric field offers an attractive route to target and activate specific chemical bonds irrespective of the bond polarity and dipole moment.[11−13] Importantly, nanostructured surfaces offer the possibility of accessing a very high electric field (10^9 V/m) with low applied voltages. Such electric tweezing has been theoretically proposed to activate unconventional reactions such as halogen bonds that are conventionally difficult.[11] Thus, the prospect of the electric field to activate conventionally stable bonds[14,15] such as C=C and N≡N and thereby lead to targeted products with high efficiency, kinetic facility, and

specificity is gaining increasing attention. This concept has also been recently explored in some heavy metal coordination complexes to understand the effect of electric field on their magnetic properties.[16,17] Application of an external electric field may influence the electronic structure and hence can change the magnetic anisotropy and magnetic exchange interactions. We computationally explored the modulating effect of the axial ligand field in lanthanide-based mononuclear single-ion magnets to achieve large magnetic anisotropy in the presence of an external electric field.[17]

Any chemical reaction involves the mass transfer of reactants and products. A specific instance when such solid-state mass transfer is directed through an external electric field is referred to as electromigration.[18] Although this is a pertinent problem in the semiconductor industry, such electric-field-induced mass transfer provides a precisely controllable route for hierarchical and arbitrary achievable nanoscale gaps.[19−21] While metals[22]

13271
https://doi.org/10.1021/acsami.1c23670
ACS Appl. Mater. Interfaces 2022, 14, 13271−13279

such as Cu, Al, and Au are susceptible to electromigration, a carbon-based metallic nanosystem such as CNTs and graphene has high resistance to electromigration owing to its strong sp^2 C=C covalent framework. The high ampacity[23] in such nanocarbons makes them ideal materials for carrying out unconventional, electric-field-induced reactions and simultaneously tracking the associated molecular pathways. The high electric field created on the surface of such dimensionally confined nanocarbons ($10^6–10^9$ V/m) is achieved at a significantly lower voltage and power (nW−μW) compared to conventional metal oxide based systems (mW−W).[24] Although such an approach is demonstrated using vertically aligned CNT arrays, the potential required ranges from 100 to 1000 V.[25,26] Therefore, a miniaturized low-power detection system for rapid sampling ultra-low concentrations of gases would be extremely desirable for applications ranging from gas chromatographic detectors to real-time on-field gas sensors. The demonstration of electric-field-directed reactions at the solid−gas heterogeneous interface opens new possibilities for the kinetic enhancement of heterogeneous catalyzed reactions such as the synthesis of ammonia.

In this direction, we showcase electric-field-driven heterogeneous solid−gas reactions on the surface of randomly oriented CNTs. The CNTs are immobilized on a chemically inert and electrically insulating matrix to form continuous, interpenetrating, and interconnected electrically conductive networks as a CNT-conductor (cCNT). Application of DC bias across the cCNT results in the simultaneous creation of (a) high electric field originating from the corrugated surface of the cCNT and (b) thermal energy due to Joule heating. The synergistic combination of these forces drives the reaction between the surface of cCNT and H_2S, thereby establishing an unnatural solid−gas heterogeneous reaction. Theoretical investigations confirm the 34% lowering of activation energy for the reaction in the presence of an applied potential of 12 V across 3 nm CNT, which generates an interfacial electric field of 4×10^9 V/m (0.008 au). The endothermicity of the reaction (0.35 eV) as estimated from DFT calculations has been conclusively established by thermometric imaging (*vide infra*). Such heterogeneous site-specific reaction with ultra-low, single-molecular concentrations of H_2S (48 ppb) is accompanied by concurrent changes in the electrical conductivity of cCNT. The structural defects on cCNT act as field trapping points and thereby form the site of such reactions, as confirmed from an excellent correlation between the defect density of cCNT (1.1×10^{11}/cm^2) and the saturating response (120 ppb) of the reaction. Moreover, the magnitude and nature of change in electrical conductivity are strongly determined by the analyte, thereby pinpointing the fundamental driving force to be the electric-field-induced site-specific reaction of cCNT. Thus, analytes such as NH_3, H_2O, N_2, and O_2 provide diametrically different signals from H_2S. This is supported by theoretical insights (*vide infra*). While the ultra-high sensitivity and specificity of the signal indicate potential gas analyzing applications, the fundamental electric-field-driven reaction mechanism established here is expected to provide transformative opportunities for several other unconventional reactions including the possibility of H_2 generation from hazardous gas sources.

cCNT exhibits the optimum combination of high specific surface area (900 m^2/g) and electrical conductivity arising from its donut-shaped electron density. Importantly, the continuous and interconnected network of CNT self-

assembled over the cellulose matrix enables uniform electrical conductivity over macroscopic length scales. This is confirmed from the invariant electrical conductivity (∼7.5 S/cm) measured across various samples and varying segments of the cCNT (Figure S1). The ultrasensitive and precise charge transduction of CNTs has been well established in field-effect transistors[27] and chemical sensors.[28,29] A majority of such applications utilize CNT as a charge-electron transducer while employing an external receptor molecule or membrane. In contrast, the current investigation aims at (a) establishing electric-field-driven unnatural reactions at the (b) solid−gas interface. While posing intrinsic challenges in charge-ordering and double-layer formation at a heterogeneous solid−gas interface, the ability to direct unnatural reactions at such an interface would provide avenues for future explorations into diverse chemical reactions of immediate significance such as NH_3 synthesis and CO_2RR.[30] In addition, the possibility of extracting the bifunctionality of the cCNT eliminates the need for a separate receptor and inspires the current investigation.

■ MATERIALS AND METHODS

Synthesis of Single Wall Carbon Nanotubes (CNTs). The carbon nanotubes employed in this work pertain to single wall carbon nanotubes prepared through a super-growth technique.[23,31−36] Briefly, the CNTs are grown in a tube furnace with Fe (3 nm) as the catalyst and acetylene acting as the carbon source. The presence of water vapor in ppm levels is established to prolong the lifetime of the catalyst and aid in the formation of monodisperse single wall carbon nanotubes (3 nm diameter) at high purity and high yield.[23,31−36]

Preparation of CNT Ink. Single walled carbon nanotubes (CNTs) are dispersed in water along with the surfactant sodium deoxycholate NaDOC. The solubility parameter of the surfactant matches that of CNTs in water; hence, it is used as the surfactant. Varying concentrations of nanotubes were added NaDOC in water to prepare 20 mg aliquots. Each aliquot was then probe-sonicated using PKS-750FM (PCI Analytics) followed by the addition of a small amount of CNTs (Table S1). Each aliquot was probe sonicated for 30 min with an "ON" time of 20 s and simultaneous "OFF" time of 10 s. As a result, the overall sonication time was 45 min for each aliquot. Depending on the total amount of CNTs added to the dispersion, 0.1 and 0.5% (weight by volume) aqueous dispersions were synthesized; these conducting inks were termed as CNT-inks.

Preparation of the CNT-Conductor (cCNT). Pristine cellulose yarns (mean diameter of 145 ± 3 μm) were obtained from the Bombay Textile Research Association. They were soaked in deionized water for 6 h and dried under ambient conditions before use. These yarns were then dip-coated with 0.1 and 0.5% CNT-ink in successive steps at a dipping rate of 2 cm/min. Each such step of dipping was followed by washing of the coated yarns, by soaking them in ethanol for 2 h, to remove NaDOC followed by drying under ambient conditions. The surfactant is removed by thorough washing of the cCNT in ethanol for 2 h followed by drying under ambient conditions (Figure S1).

The samples thus prepared exhibited finite electrical conductivity (7.5 S/cm) indicating a strong, continuously interpenetrating network of CNTs immobilized on the matrix, termed as cCNT. Further increase in conductivity was affected by the exposure of the yarns to sulfuric acid (H_2SO_4). Acid exposure leads to −COOH and −OH functionalization of CNTs. This leads to the saturation of some C centers that bear the acid group, thus creating defects in the sp^2 C network in CNTs. This, in turn, leads to an ease in the hole doping mechanism of charge conduction and facilitates a drastic increase of conductivity. Such −OH and −COOH functionalized cCNTs are employed in control experiments.

Fabrication of the CNT Gas Sensor Device. The change in resistivity with time of cCNT was observed in the presence of air and in vacuum for comparison. It was then fixed in a pre-vacuumed gas
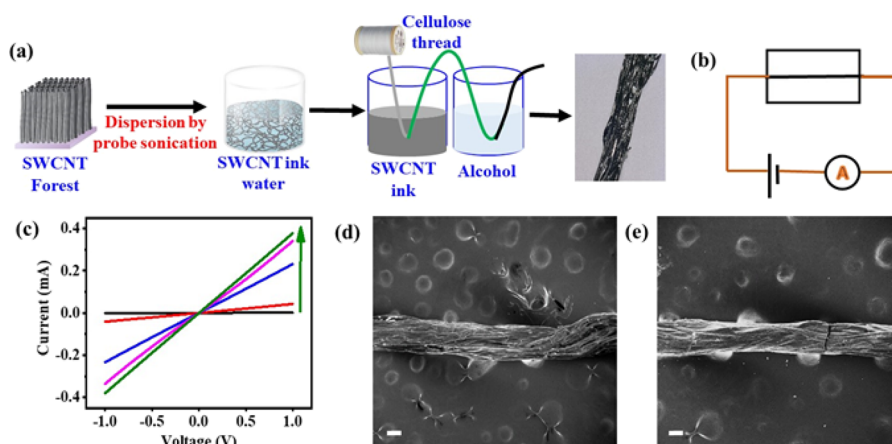
Figure 1. (a) Schematic sequence of steps for the fabrication of cCNT. (b) Circuit for the measurement of electrical properties. (c) Current−voltage plot recorded at various stages of the fabrication of cCNT from the pristine cellulose thread (color code: black, cellulose thread; red, first dipping in 0.1% CNT-ink dispersion; blue, second dipping and ethanol wash; pink, third dipping and ethanol wash; and green, fourth dipping in 0.5% CNT-ink dispersion and ethanol wash). FE-SEM images of the (d) pristine cCNT and (e) breakdown observed after applying over the threshold voltage of 16 V (scale bar: 100 μm).

sensing setup, which helped in observing the change in resistivity of cCNT with time in the presence of different gases like N_2, O_2, H_2S, H_2O vapor, and NH_3.

Gas Sensing Setup. For in situ generation of H_2S, 15% HCl in a separating funnel was poured dropwise over powdered FeS placed in a two-necked RB flask. The generated gas was passed over to the connected Schlenk line, and the amount or concentration of H_2S (mm Hg/ppb) to be input into the pre-vacuumed setup was controlled manually through a valve, monitored by a manometer in terms of mm Hg. The sensing device inside the setup was attached to a DC voltage supply and a multimeter for electrical measurements (Figure S8). The change in resistivity with respect to time was calculated after applying 75% of the breakdown voltage to the device for different H_2S gas concentrations (ppb). Similarly, the experiments were done in the presence of air, vacuum, NH_3, and H_2O vapors for comparison.

Characterization. Scanning electron microscopy images of cCNT were carried out in a JEOL JSM-7600F FEG-SEM instrument. Electrochemical data were recorded using a Biologic SP 300 electrochemical workstation. I−V characteristics of the cCNT were recorded for different concentrations of gas. The treated threads were analyzed to see changes in chemical bonding using X-ray photo-electron spectroscopy (Axis Supra Model, SHIMADZU group).

RESULTS AND DISCUSSION

Pristine CNTs are synthesized through the water-assisted, super-growth chemical vapor deposition route that provides uniform and mono-disperse single walled carbon nanotubes (CNTs) with an average diameter of 3 ± 0.3 nm and length of 400 μm. The pristine CNTs are characterized through both microscopic and spectroscopic techniques (Figure S11). The cCNT is fabricated through a series of steps involving (i) the formation of an aqueous dispersion of CNT-ink[33,34] and (ii) dip-coating pristine cellulose yarns through the CNT-ink followed[33,34,37,38] by (iii) the removal of the anionic stabilizer[39] (NaDOC, Figure 1a and Figure S1). Such a scalable and facile approach results in the enhancement of the electrical conductivity of the CNT-coated cellulose yarn (cCNT) by $\sim 10^{15}$ times when compared to the pristine cellulose yarn. Importantly, the ohmic conductance is further improved by $\sim 42\%$ after treating the cCNT in ethanol, which acts to remove the surfactant (step iii) and thereby lowers the junction resistance between the interconnected CNT (Figure 1a,c). These cyclic processes (steps ii and iii) are repeated to

create multilayer interconnected networks of CNT, resulting in an electrical conductivity of ~ 7.5 S/cm. While a single dipping was sufficient to coat CNTs on the cellulose thread and make it electrically conductive. However, the electrical conductivity measured from various segments of the same sample and across multiple similar samples showed variations in electrical conductivity.

This is attributed to the non-uniformity in the CNT coating and the resulting inconsistency in the number of inter-CNT junctions formed. Repeated dipping−washing−drying cycles were carried out to remove any such inconsistency and achieve uniform electrical conductivity (7.5 S/cm). The uniformity of coating and the number of inter-CNT junctions reached a saturation value with increase in the CNT loading. As seen from Figure S2, the electrical conductivity shows a saturation with increased CNT loading (0.125 mg/cm) and did not change beyond that. It is important to note that such stabilization of electrical conductivity over the macroscopic length scales (over 10 cm) of the cCNT conductor is achieved at ultra-low levels of CNT loading (0.125 mg/cm) due to the long aspect ratio (10^5) of the CNTs and their ability to form dendritic interconnected networks.[40]

The surface of cCNT exhibits the presence of a uniformly immobilized interpenetrating network of CNT and thereby behaves as an ohmic conductor with monotonic, linear current−voltage dependence (Figure 1c). This ensures unchanged electrical conductivity over length scales (10 cm) that are typically 4 orders of magnitude higher than the dimension of individual CNTs (500 μm). Further, the uniform coverage produces sharp surface features arising from individual CNTs. This mimics the action of points in a lightning conductor and thereby enables intense concentrated electric fields ($\sim 4 \times 10^9$ V/m) that are at least 5 orders of magnitude higher than those observed in conventional metallic conductors.[23,41] In addition to such high electric field flux, localized thermal heating also operates in the CNT due to its finite ohmic resistance. The combination of both high electric field and Joule heating creates chemically reactive sites on the surface of the cCNT.

Accordingly, a chemresistor device is fabricated with the cCNT acting as both the sensing and transducing elements

(Figure 1b,d). It is noteworthy that a DC bias of 16 V is able to cause the complete rupture of cCNT (Figure 1e). Therefore, all experiments are conducted at 75% of 16 V to avoid such failures. Experiments conducted at a constant DC bias (12 V) with N_2/O_2 as the carrier gas and vacuum (50 mm Hg) exhibit a delayed time response leading to a minor (2−4%) increase in the electrical resistivity of the chemresistor (Figure 2a).
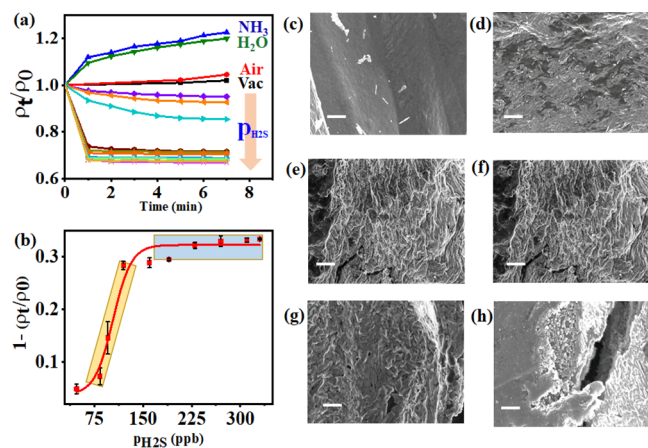
Figure 2. (a) Time evolution of the resistivity of cCNT in the ambience of different analytes (NH_3, water vapor, air, and vacuum) and increasing concentrations of H_2S. (b) Sensitivity of the conductor in different concentrations of H_2S. FESEM image of cCNT exposed to H_2S of concentration (c) 48 ppb, (d) 84 ppb, (e) 96 ppb, (f) 120 ppb, (g) 190 ppb, and (h) 310 ppb. Scale bar: 2 μm.

Control experiments that were carried out by replacing the sensing element (cCNT) with metallic Cu wire failed to produce any observable change in resistivity, indicating the decisive role of cCNT. Additionally, control experiments were carried out by applying a low, subthreshold potential difference (0.5 V) to the cCNT, wherein no perceivable changes in resistivity were observed either under varied concentrations of H_2S (75 and 500 ppb, Figure S3) or at ambient conditions (Figure S10). This confirms the mandatory requirement of an electric field for the solid−gas reaction to occur. Further, identical I−V measurements in the presence of an electric field (∼4 × 10⁹ V/m) were carried out with cCNTs functionalized with −OH and −COOH groups through treatment in H_2SO_4 (Figure S3). Consistent with earlier observations, the resistivity of the device did not exhibit any noticeable changes in the presence of 150 ppb of H_2S (Figure S3). Taken together, these control experiments confirmed the importance of both pristine cCNT and electric field in the observations.

To probe the effect of other gases, identical experiments were conducted under controlled relative humidity (40%). The time evolution of resistivity showed a significantly sharp increase in the first 60 s of exposure followed by saturation. An identical trend was observed in experiments conducted with NH_3 as the analyte (Figure 2a). Thereby, the ultra-high sensitivity and the signal response of cCNT to its immediate environment are established. The sensitivity obtained here compares with that of gas chromatographic detectors, while the time taken for signal stabilization is ∼100 s. An identical yet diametrically opposite trend obtained with NH_3 and humidity clearly indicates the role of chemical charge transfer in the observed changes in resistivity. Both H_2O and NH_3 lead to charge injection at the active sites of cCNT generated by the

intense electric field and localized thermal energy. These observations encouraged further investigations into the sensitivity of cCNT toward H_2S.

Hydrogen sulfide (H_2S) is a toxic and inflammable gas that also doubles as an agricultural marker in paddy fields. The precise detection of H_2S poses a significant challenge due to a major interferon in the form of moisture. Therefore, developing an ultra-sensitive and chemospecific sensor for H_2S would immensely benefit these two contrasting and critical aspects.

Inspired by this, the chemoresistive sensor−transducer platform (cCNT) is subjected to systematic variation in the concentration of H_2S (pH_2S) changing from 48 to 330 ppb (Figure 2b). The relative change in resistance is observed to follow a sigmoidal behavior with two clear domains (Figure 2b). An induction domain at H_2S concentrations below 75 ppb is observed. Since the site-specific solid−gas interfacial reaction is established as the mechanism of sensing (*vide infra*), the induction concentration refers to the minimum number of active sites on the cCNT conductor that need to participate in the solid−gas reaction for the change in resistivity to manifest at the device level. Thus, the induction concentration of <75 ppb is also in agreement with the defect density of the cCNT conductor (1.1 × 10¹¹/cm²), as estimated from Raman measurements. The initial domain 1 (yellow, Figure 2b) exhibits a linear increase in resistivity and occurs between pH_2S of 48 and 120 ppb. Beyond this, domain 2 (blue, Figure 2b) is marked by the saturation of the signal response and extends up to pH_2S of 330 ppb. The observed saturation in the signal from the cCNT corresponds to the saturation of its surface with H_2S. The Stone−Wales defect centers on the cCNT act as pinning points[42] for the π-electron charge density and hence form the preferred reactive sites.

Importantly, the saturation observed beyond 120 ppb is in excellent agreement with the defect density estimated from Raman spectra. Detailed DFT calculations (*vide infra*) show that the defect sites are important for the reaction to proceed, and therefore, a pristine cCNT with no defect is unlikely to be reactive. As the defect sites are limited, after 120 ppb pH_2S, the saturation occurs as all the defect sites are encaged with the H_2S. Systematic and calibrated exposure to H_2S results in a proportionate increase in the roughness of cCNT. (Figure S4 and Figure 2c−h). Thus, the kinetics of response and the morphological changes observed point to the critical role of surface sites on the cCNT. This is further investigated through surface sensitive X-ray photoelectron spectroscopy (XPS). The pristine cCNT exhibits the characteristic binding energy component at 284.6 eV arising from the characteristic sp² C═C framework (Figure 3a). Given the complexity of the system, careful control experiments and analysis are warranted. In this direction, the O 1s region of the as-prepared pristine CNT powder and cCNT is compared (Figure S5). Importantly, the XPS of the as-synthesized CNT powder did not show the presence of any O 1s peak, reaffirming our interpretation. This confirms that the C═O peak observed in cCNT is exclusively due to the cellulose substrate and not from the CNTs themselves. In addition, the O 1s XPS in cCNT has been analyzed and found to be consistent both before and after exposure to H_2S (Figure S6). Consequently, the pristine cCNT does not exhibit any peak corresponding to S 2p, in contrast to clear signatures observed for the same sample after exposure to H_2S (Figure 3b). Accordingly, S 2p$_{3/2}$ and S 2p$_{1/2}$ are observed at 163.8 and 165 eV, respectively. The prominent peak at
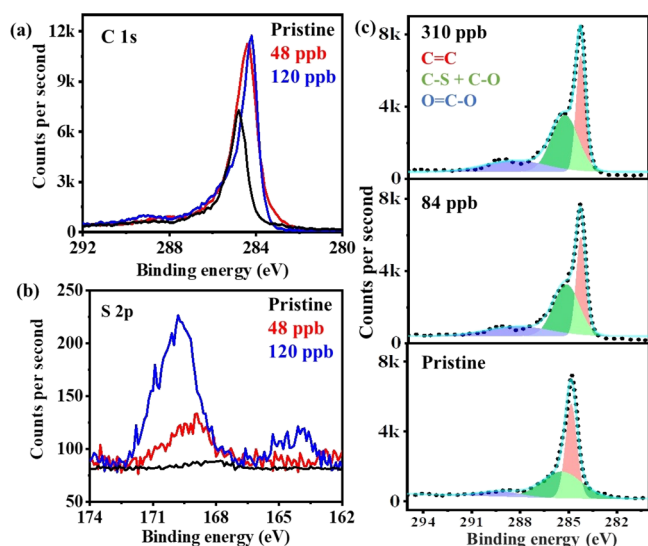
Figure 3. XPS spectra of (a) C 1s and (b) S 2p of exposed cCNT. (c) Deconvolution of C 1s spectra showing the evolution of the C−S peak after exposure to H$_2$S.

higher binding energy corresponds to the presence of sulfate species (SO$_4^{2-}$) and is corroborated by the EDS analysis (Figure S7). Furthermore, the C 1s region of the samples provides in-depth information on the nature and site of the solid−gas reaction. The presence of O=C−O at 288.9 eV in pristine cCNT and its increasing peak intensity upon exposure to H$_2$S suggest the binding of sulfur on the cCNT surface. While the peaks at 285.6 and 286.5 eV correspond to C−S and C−O, respectively, these peaks are consistently observed in all the samples exposed to H$_2$S, making it challenging to pinpoint the exact nature of the reaction site.[42] Furthermore, the diffusion of gaseous H$_2$S and the skin-depth of XPS used to probe the surface chemistry are expected to be similar, and therefore, it is challenging to pinpoint the exact site of the reaction. Finally, the survey spectra, O 1s spectra, and their quantification before and after exposure to H$_2$S concur with

the experimental understanding (Figure S8). Therefore, we propose that both the C−S bond and the participation of −COOH (from substrate) result in these XPS observations.

The thermodynamics of this reaction are captured by in situ monitoring of the surface temperature at the reaction site. Infrared-based thermometry (Figure 4a,c) indicates an increase in the surface temperature of the cCNT under the influence of the electric field (5 V), originating from Joule heating (Figure 4b). In a vacuum, this temperature difference (ΔT) stabilizes within 60 s, which is in excellent agreement with the time response of the sensor (Figure 2a). Subsequent exposure to H$_2$S results in a significant lowering of the surface temperature to below room temperature (ΔT = −6 °C) (Figure 4b). This response is unique to H$_2$S among the several analytes and controls tested and thereby rules out the possibility of radiative heat transfer. Further, the temperature of the cCNT stabilizes below room temperature for over 120s. This time scale is in good agreement with the time scale observed for signal saturation in Figure 4c. Thus, the lowering of temperature points to the endothermic reaction between H$_2$S and cCNT, which is confirmed from XPS measurements (*vide supra*). The temperature profile increases beyond 3 min, indicating the completion of the reaction. Moreover, such a reaction between H$_2$S and cCNT is repeatable, with periodic and precise changes in the temperature of the cCNT for every pulsing of the analyte (H$_2$S).

■ THEORETICAL STUDIES

Density functional theory (DFT) calculations have been carried out in the gas phase in both the presence and absence of an oriented external electric field (OEEF) to gain insight into the mechanistic aspects of the above reaction and to rationalize various experimental observations. All the calculations have been carried out in a small CNT model with chirality (5,5) (for further details, see computational details in the Supporting Information). To begin with, we have optimized the structure of O$_2$ adsorbed on the CNT using DFT (B3LYP/6-31G(d,p)) in a pristine environment and then
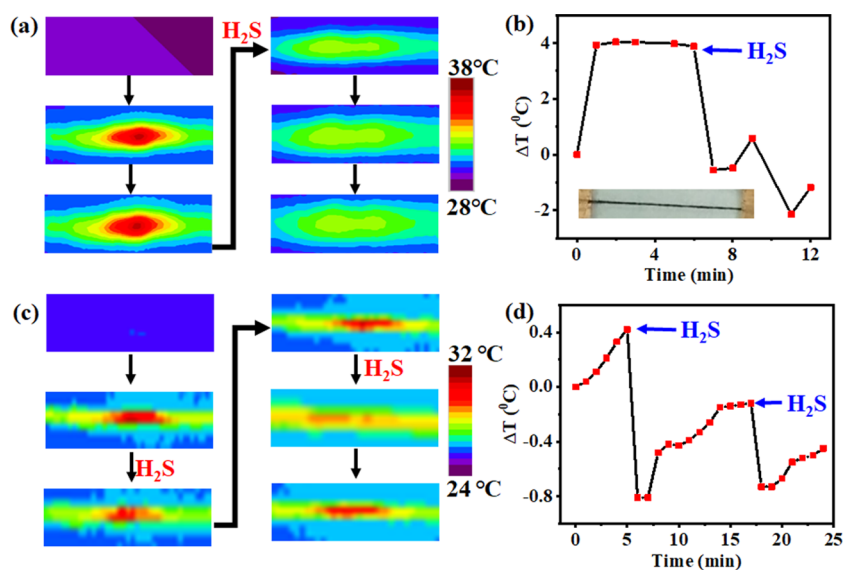
Figure 4. Thermal images of heating of cCNT when applied to 5 V with (a) one cycle and (c) two cycles of exposure to H$_2$S. (b and d, respectively) The drop in temperature after exposure to H$_2$S shows the endothermic behavior of the reaction (inset photo of cCNT with Cu tape ends).
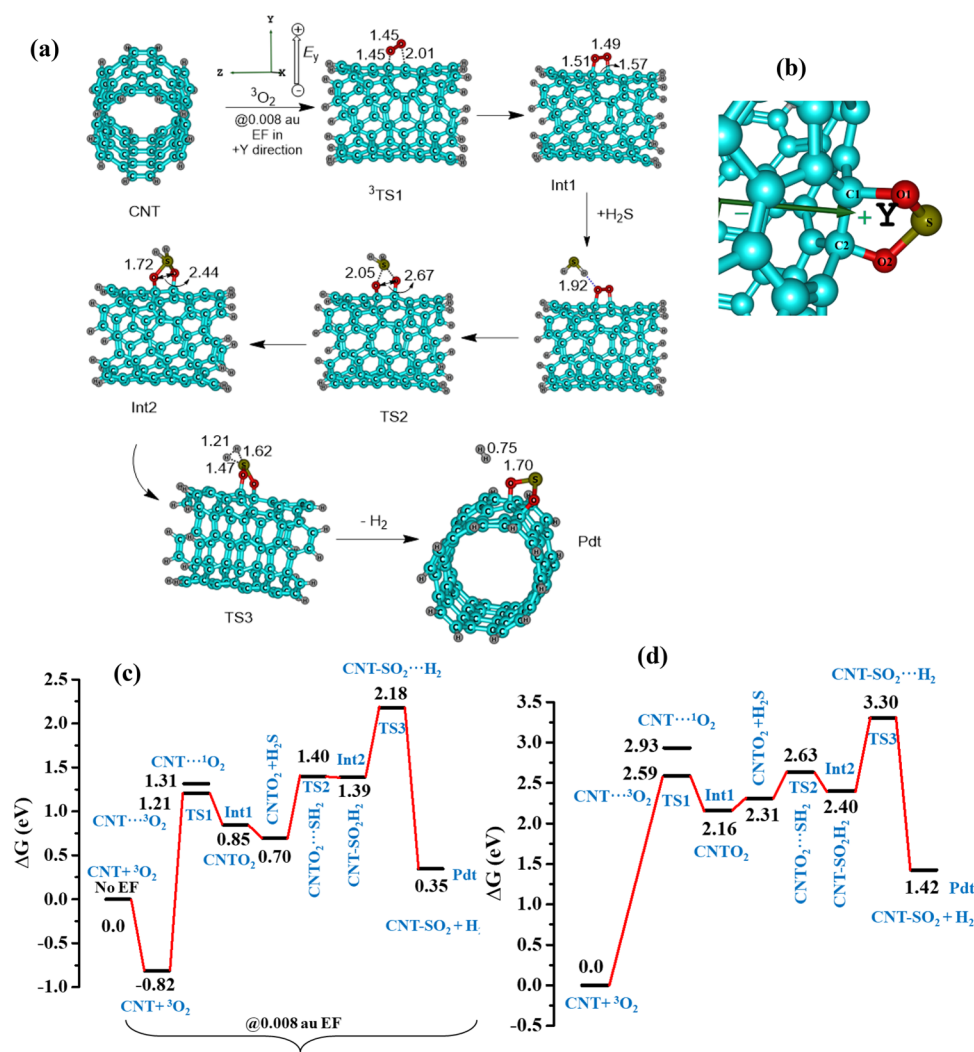
Figure 5. (a) Reaction mechanism or pathway obtained from the DFT method with the important bond lengths in angstrom (Å) unit in the presence of 0.008 au OEEF and (b) enlarged view at the reaction site with atom numbers and OEEF direction. (c) Gibbs free energy profile diagram of the reactant, product, and transition states of the same reaction in eV scale and (d) the same reaction mechanism in the absence of any electric field.

used the same structure to apply an electric field in a certain direction to estimate the binding affinity in the presence of an external electric field. While O_2 is found to favorably bind to CNT in the absence of applied electric field, when an OEEF of 0.008 au (atomic unit; 1 au = 51.4 V/Å) along the perpendicular direction of CNT (here +Y direction; Figure 5a,b) is applied, the binding is estimated to be much more favorable (by ∼0.8 eV or 18 kcal/mol). This may be attributed to the increased polarity and dipole moment of the overall nanotube in the presence of OEEF (Tables S2−S4). At first, the oxygen from the air is expected to bind preferably to the defected site on the CNT surface.[43] We have estimated the transition state for the formation of the C_{CNT}···O=O bond, and this is found to be a concerted transition state occurring on the triplet spin surface (TS1) with an estimated barrier height of 1.21 eV (27.8 kcal/mol) with respect to the reactants at zero OEEF (Figure 5c,d and Figures S12 and S13). While we cannot rule out the possibility that the oxygen might have adsorbed on the CNT surface prior to the applied electric field, in the presence of OEEF, the kinetic barriers are eased significantly, facilitating stronger binding.

At the transition state, the O···O bond length increases from 1.21 Å in the native state to 1.45 Å at TS1, suggesting the cleavage of the O=O π bond leaving a significant radical character at the O_2 (spin density ∼0.34 detected) atom sites. After the transition state, the formation of an intermediate (Int1) wherein the O_2 bound to SWCNT is assumed where the O···O bond length is estimated to be 1.49 Å, revealing the partial cleavage of the double bond character of the O_2 upon adsorption. In the next step, H_2S is expected to approach and form a weak complex having a strong hydrogen bonding interaction between the H1 of the H_2S and the adsorbed oxygen (H···O distance is 1.92 Å), and this yields a weak complex that is exothermic in its formation by −0.15 eV with respect to the CNT-O_2 adduct (Figure 5a). In the next step, sulfur insertion between the weaker O···O bond is assumed to take place via a concerted transition state (TS2) with an energy barrier of 1.4 eV (32.2 kcal/mol). At this transition state, the S−O bond is only partially formed, and the S−H bonds are elongated (S−O distance is 2.05 Å, and S−H distances are 1.36−1.40 Å; also see Table S2 in the Supporting Information). In the next step, the S−O bond formation is complete (Int2), and the formation of this intermediate is

found to be relatively endergonic by 1.39 eV (32.1 kcal/mol), suggesting that this is unlikely to be stable and is expected to undergo a further transformation. The attack of sulfur on the weakened O···O bond is found to be facilitated by the presence of OEEF as the same kinetic barrier in the absence of OEFF is found to be ∼1.2 eV higher, rationalizing the need for the electric field to facilitate such a difficult transformation (Figure 5c,d and Figures S12 and S13).

In the next step, the elimination of H_2 from Int2 is assumed to take place via TS3, leading to the final product. The H_2 elimination transition state (TS3) passes through a very high energy barrier of 2.18 eV (50.2 kcal/mol) also in a concerted fashion. Such a high barrier suggests that this step is the rate-limiting step in the reaction profile (Figure S13). The final product (Pdt) that is the sulfoxide adduct and the H_2 molecule is slightly endergonic (0.35 eV or 8.0 kcal/mol; Figure S13).The S−O bond length is estimated to be 1.7 Å in the final product formation. The computed PES surface suggests that the overall reaction is endergonic, and this is consistent with experiments where exposure of CNT to H_2S results in a significant lowering of the surface temperature.

To assess the importance of the electric field in facilitating the reaction, we have carried out the PES calculation using the same schematic mechanism in the absence of OEEF (Figure 5c,d and Figures S12 and S13) and found that all the reactants, intermediates, and transition states are significantly destabilized by more than 1.0 eV compared to the PES computed in the presence of OEEF. Most importantly, the TS3 passes through an energy barrier of 3.30 eV (76.1 kcal/mol) energy, which practically eliminates the possibility of this reaction occurring in the absence of an electric field. The changes in the structural parameters, NPA (natural population analysis) charges from NBO calculations, and dipole moment comparison have been made with and without the 0.008 au OEEF (Tables S3 and S4). The total dipole moment is directed perpendicular to the CNT (Figure 5b). The increased dipole moment along the +Y direction indicates that in the presence of an electric field, the reactions proceed via a pathway that creates a significant polarity leading to this rather unusual splitting of H_2S, which is otherwise a cumbersome reaction given the very high bond-dissociation energy (Do-(HS-H) = 90 kcal/mol and $\Delta H(H_2S)$ = 175.5 kcal/mol).[44−46] Furthermore, we have also plotted the electrostatic potential surface diagram to visualize the change in charge density while applying the electric field in the gas phase perpendicular to the CNT, and this clearly reveals the enhancement in the polarization of atoms/bond charges in the presence of OEEF, affirming our points (Figure S14). The application of the electric field in the pristine CNT clearly shows a strong contrast in charge separation, which is helping in O_2 binding. Also, in the final product, the charge separation is more prominent in the presence of an electric field compared to that in the absence of an electric field (Figure S14c−f). The theoretical reaction scheme presented here has been modeled in the presence of aerial oxygen; however, the other aerial species such as moisture (H_2O), hydroxide, and acidic ions could also be present[41] and hence can participate in facilitating the H_2S binding and SO_2 adduct formation. Modeling the reaction in the presence of $OH^−$ ions has also been attempted with DFT methods in the presence of OEEF. It was found that after the binding of two $OH^−$ ions to the neutral SWCNT, the binding of H_2S was energetically unfavorable of passes through an intermediate that has energy close to 3.5 eV (see Figure S15 in the Supporting Information).

Additionally, we have also computed the Raman frequencies of the pristine CNT as well as the final product. As expected for the pristine CNT, the ring C−C stretching and C−H bending occur at around 860 to 1600 $cm^{−1}$, and the C−H stretching takes place at more than 3000 $cm^{−1}$. Similar peaks have been observed in the case of S-CNT (product). The SO_2 group bending vibrations are prominent at less than 1000 $cm^{−1}$ and are Raman inactive. The DFT computed Raman spectra match quite nicely with the experimental Raman spectra (Figure S17 and Tables S5 and S6). Furthermore, the total density of states (TDOS) and partial DOS have also been plotted for the pristine CNT, SWCNT, Int1 (O_2 adduct), and final SO_2 adduct in Figures S12−S18 in the Supporting Information.

■ CONCLUSIONS

In summary, we illustrate the use of the electric field to manipulate and drive unconventional chemical reactions at the heterogeneous solid−gas interface of nanomaterials. The defect centers have been proven to be more prone to such reactions through a combination of spectroscopic, thermometric, and theoretical insights. Such reactions induced distinct and unique changes in the electronic structure of the nanomaterials, leading to interesting opportunities to use such ensembles as mimics of gas chromatographic systems. Further, thermometric investigations pinpoint the enthalpy-driven changes at the defect sites, providing observations that are directly supported by theoretical calculations. Finally, the prospect of carrying out chemical-specific and site-oriented reactions using the external electric field opens newer possibilities for the manipulation of electronic structure in nanomaterials, leading to diverse applications in energy, catalysis, and sensing based devices.

■ ASSOCIATED CONTENT

ⓢ Supporting Information

The Supporting Information is available free of charge at https://pubs.acs.org/doi/10.1021/acsami.1c23670.

> Preparation and characterization of cCNT exposed to H_2S; experimental setup; transition state optimizations; comparison between the results obtained from experiment and theoretical calculations; and electronic energy profile diagram (PDF)

■ AUTHOR INFORMATION

Corresponding Authors

Gopalan Rajaraman − *Department of Chemistry, Indian Institution of Technology Bombay, Mumbai 400076 Maharashtra, India;* ⓞ orcid.org/0000-0001-6133-3026; Email: rajaraman@chem.iitb.ac.in

Chandramouli Subramaniam − *Department of Chemistry, Indian Institution of Technology Bombay, Mumbai 400076 Maharashtra, India;* ⓞ orcid.org/0000-0001-8335-7395; Email: csubbu@chem.iitb.ac.in

Authors

Itisha Dwivedi − *Department of Chemistry, Indian Institution of Technology Bombay, Mumbai 400076 Maharashtra, India*

Arup Sarkar − *Department of Chemistry, Indian Institution of Technology Bombay, Mumbai 400076 Maharashtra, India*

Complete contact information is available at:
https://pubs.acs.org/10.1021/acsami.1c23670

Author Contributions

I.D. carried out the experimental measurements and data analysis. A.S. carried out the theoretical studies and analysis. G.R. and C.S. conceptualized the studies and discussed the results. All authors co-wrote the manuscript.

Notes

The authors declare no competing financial interest.

■ ABBREVIATIONS

CNT, carbon nanotube
SWCNT, single walled carbon nanotube
OEEF, oriented external electric field

■ REFERENCES

(1) Rebreyend, C.; De Bruin, B. Photolytic N_2 Splitting: A Road to Sustainable NH_3 Production? *Angew. Chem., Int. Ed.* **2015**, *54*, 42−44.

(2) Zhang, L.; Ji, X.; Ren, X.; Ma, Y.; Shi, X.; Tian, Z.; Asiri, A. M.; Chen, L.; Tang, B.; Sun, X. Electrochemical Ammonia Synthesis via Nitrogen Reduction Reaction on a MoS_2 Catalyst: Theoretical and Experimental Studies. *Adv. Mater.* **2018**, *30*, 1800191.

(3) Zhang, L.; Ji, X.; Ren, X.; Luo, Y.; Shi, X.; Asiri, A. M.; Zheng, B.; Sun, X. Efficient Electrochemical N_2 Reduction to NH_3 on MoN Nanosheets Array under Ambient Conditions. *ACS Sustainable Chem. Eng.* **2018**, *6*, 9550−9554.

(4) Liu, Y.; Su, Y.; Quan, X.; Fan, X.; Chen, S.; Yu, H.; Zhao, H.; Zhang, Y.; Zhao, J. Facile Ammonia Synthesis from Electrocatalytic N_2 Reduction under Ambient Conditions on N-Doped Porous Carbon. *ACS Catal.* **2018**, *8*, 1186−1191.

(5) Li, X.; Li, T.; Ma, Y.; Wei, Q.; Qiu, W.; Guo, H.; Shi, X.; Zhang, P.; Asiri, A. M.; Chen, L.; Tang, B.; Sun, X. Boosted Electrocatalytic N_2 Reduction to NH_3 by Defect-Rich MoS_2 Nanoflower. *Adv. Energy Mater.* **2018**, *8*, 1−8.

(6) Maye, M. M.; Lou, Y.; Zhong, C. J. Core-Shell Gold Nanoparticle Assembly as Novel Electrocatalyst of CO Oxidation. *Langmuir* **2000**, *16*, 7520−7523.

(7) Fortunato, G.; Oswald, H. R.; Reller, A. Spinel-Type Oxide Catalysts for Low Temperature CO Oxidation Generated by Use of an Ultrasonic Aerosol Pyrolysis Process. *J. Mater. Chem.* **2001**, *11*, 905−911.

(8) Nie, L.; Mei, D.; Xiong, H.; Peng, B.; Ren, Z.; Hernandez, X. I. P.; DeLaRiva, A.; Wang, M.; Engelhard, M. H.; Kovarik, L.; Datye, A. K.; Wang, Y. Activation of Surface Lattice Oxygen in Single-Atom Pt/CeO_2 for Low-Temperature CO Oxidation. *Science* **2017**, *358*, 1419−1423.

(9) Joo, S. H.; Park, J. Y.; Tsung, C. K.; Yamada, Y.; Yang, P.; Somorjai, G. A. Thermally Stable Pt/Mesoporous Silica Core-Shell Nanocatalysts for High-Temperature Reactions. *Nat. Mater.* **2009**, *8*, 126−131.

(10) Salvatore, K. L.; Deng, K.; Yue, S.; Mcguire, S. C.; Rodriguez, J. A.; Wong, S. S. Optimized Microwave-Based Synthesis of Thermally Stable Inverse Catalytic Core-Shell Motifs for CO2Hydrogenation. *ACS Appl. Mater. Interfaces* **2020**, *12*, 32591−32603.

(11) Shaik, S.; Danovich, D.; Joy, J.; Wang, Z.; Stuyver, T. Electric-Field Mediated Chemistry: Uncovering and Exploiting the Potential of (Oriented) Electric Fields to Exert Chemical Catalysis and Reaction Control. *J. Am. Chem. Soc.* **2020**, *142*, 12551−12562.

(12) Wang, C.; Danovich, D.; Chen, H.; Shaik, S. Oriented External Electric Fields: Tweezers and Catalysts for Reactivity in Halogen-Bond Complexes. *J. Am. Chem. Soc.* **2019**, *141*, 7122−7136.

(13) Shaik, S.; Ramanan, R.; Danovich, D.; Mandal, D. Structure and Reactivity/Selectivity Control by Oriented-External Electric Fields. *Chem. Soc. Rev.* **2018**, *47*, 5125−5145.

(14) Behler, K.; Osswald, S.; Ye, H.; Dimovski, S.; Gogotsi, Y. Effect of Thermal Treatment on the Structure of Multi-Walled Carbon Nanotubes. *J. Nanopart. Res.* **2006**, *8*, 615−625.

(15) Jung, H. Y.; Araujo, P. T.; Kim, Y. L.; Jung, S. M.; Jia, X.; Hong, S.; Ahn, C. W.; Kong, J.; Dresselhaus, M. S.; Kar, S.; Jung, Y. J. Sculpting Carbon Bonds for Allotropic Transformation through Solid-State Re-Engineering of -Sp 2 Carbon. *Nat. Commun.* **2014**, *5*, 1−8.

(16) Fittipaldi, M.; Cini, A.; Annino, G.; Vindigni, A.; Caneschi, A.; Sessoli, R. Electric Field Modulation of Magnetic Exchange in Molecular Helices. *Nat. Mater.* **2019**, *18*, 329−334.

(17) Sarkar, A.; Rajaraman, G. Modulating Magnetic Anisotropy in Ln(Iii) Single-Ion Magnets Using an External Electric Field. *Chem. Sci.* **2020**, *11*, 10324−10330.

(18) Ho, P. S.; Kwok, T. Electromigration in Metals. *Rep. Prog. Phys.* **1989**, *52*, 301−348.

(19) Collins, P. G.; Hersam, M.; Arnold, M.; Martel, R.; Avouris, P. Current Saturation and Electrical Breakdown in Multiwalled Carbon Nanotubes. *Phys. Rev. Lett.* **2001**, *86*, 3128−3131.

(20) Taychatanapat, T.; Bolotin, K. I.; Kuemmeth, F.; Ralph, D. C. Imaging Electromigration during the Formation of Break Junctions. *Nano Lett.* **2007**, *7*, 652−656.

(21) Ward, D. R.; Grady, N. K.; Levin, C. S.; Halas, N. J.; Wu, Y.; Nordlander, P.; Natelson, D. Electromigrated Nanoscale Gaps for Surface-Enhanced Raman Spectroscopy. *Nano Lett.* **2007**, *7*, 1396−1400.

(22) Wilhite, P.; Vyas, A. A.; Tan, J.; Tan, J.; Yamada, T.; Wang, P.; Park, J.; Yang, C. Y. Metal-Nanocarbon Contacts. *Semicond. Sci. Technol.* **2014**, *29*, No. 054006.

(23) Subramaniam, C.; Yamada, T.; Kobashi, K.; Sekiguchi, A.; Futaba, D. N.; Yumura, M.; Hata, K. One Hundred Fold Increase in Current Carrying Capacity in a Carbon Nanotube-Copper Composite. *Nat. Commun.* **2013**, *4*, 1−7.

(24) Kim, H.; Jin, C.; Park, S.; Kim, S.; Lee, C. H 2S Gas Sensing Properties of Bare and Pd-Functionalized CuO Nanorods. *Sens. Actuators, B* **2012**, *161*, 594−599.

(25) Ozden, S.; Brunetto, G.; Karthiselva, N. S.; Galvão, D. S.; Roy, A.; Bakshi, S. R.; Tiwary, C. S.; Ajayan, P. M. Controlled 3D Carbon Nanotube Structures by Plasma Welding. *Adv. Mater. Interfaces* **2016**, *3*, 1−8.

(26) Hawtof, R.; Ghosh, S.; Guarr, E.; Xu, C.; Sankaran, R. M.; Renner, J. N. Catalyst-Free, Highly Selective Synthesis of Ammonia from Nitrogen and Water by a Plasma Electrolytic System. *Asian J. Chem.* **2019**, *5*, No. eaat5778.

(27) Pesetski, A. A.; Baumgardner, J. E.; Folk, E.; Przybysz, J. X.; Adam, J. D.; Zhang, H. Carbon Nanotube Field-Effect Transistor Operation at Microwave Frequencies. *Appl. Phys. Lett.* **2006**, *88*, 1−4.

(28) Ji, Q.; Honma, I.; Paek, S. M.; Akada, M.; Hill, J. P.; Vinu, A.; Ariga, K. Layer-by-Layer Films of Graphene and Ionic Liquids for Highly Selective Gas Sensing. *Angew. Chem., Int. Ed.* **2010**, *49*, 9737−9739.

(29) Drera, G.; Freddi, S.; Emelianov, A. V.; Bobrinetskiy, I. I.; Chiesa, M.; Zanotti, M.; Pagliara, S.; Fedorov, F. S.; Nasibulin, A. G.; Montuschi, P.; Sangaletti, L. Exploring the Performance of a Functionalized CNT-Based Sensor Array for Breathomics through Clustering and Classification Algorithms: From Gas Sensing of

Selective Biomarkers to Discrimination of Chronic Obstructive Pulmonary Disease. *RSC Adv.* **2021**, *11*, 30270−30282.

(30) Wu, J.; Sharifi, T.; Gao, Y.; Zhang, T.; Ajayan, P. M. Emerging Carbon-Based Heterogeneous Catalysts for Electrochemical Reduction of Carbon Dioxide into Value-Added Chemicals. *Adv. Mater.* **2019**, *31*, 1−24.

(31) Futaba, D. N.; Hata, K.; Yamada, T.; Hiraoka, T.; Hayamizu, Y.; Kakudate, Y.; Tanaike, O.; Hatori, H.; Yumura, M.; Iijima, S. Shape-Engineerable and Highly Densely Packed Single-Walled Carbon Nanotubes and Their Application as Super-Capacitor Electrodes. *Nat. Mater.* **2006**, *5*, 987−994.

(32) Hata, K.; Futaba, D. N.; Mizuno, K.; Namai, T.; Yumura, M.; Iijima, S. Water-Assisted Highly Efficient Synthesis of Impurity-Free Single-Walled Carbon Nanotubes. *Science* **2004**, *306*, 1362−1364.

(33) Moronshing, M.; Subramaniam, C. Scalable Approach to Highly Efficient and Rapid Capacitive Deionization with CNT-Thread As Electrodes. *ACS Appl. Mater. Interfaces* **2017**, *9*, 39907−39915.

(34) Jha, M. K.; Hata, K.; Subramaniam, C. Interwoven Carbon Nanotube Wires for High-Performing, Mechanically Robust, Washable, and Wearable Supercapacitors. *ACS Appl. Mater. Interfaces* **2019**, *11*, 18285−18294.

(35) Mondal, S.; Subramaniam, C. Point-of-Care, Cable-Type Electrochemical Zn^{2+} Sensor with Ultrahigh Sensitivity and Wide Detection Range for Soil and Sweat Analysis. *ACS Sustainable Chem. Eng.* **2019**, *7*, 14569−14579.

(36) Kalyani, V.; Mondal, S.; Saha, J.; Subramaniam, C. Electrochemical, Top-down Nanostructured Pseudocapacitive Electrodes for Enhanced Specific Capacitance and Cycling Efficiency. *Nanoscale* **2018**, *10*, 3663−3672.

(37) Jha, M. K.; Jain, T.; Subramaniam, C. Origami of Solid-State Supercapacitive Microjunctions Operable at 3 V with High Specific Energy Density for Wearable Electronics. *ACS Appl. Electron. Mater.* **2020**, *2*, 659−669.

(38) Jha, M. K.; Ball, R.; Seelaboyina, R.; Subramaniam, C. All Solid-State Coaxial Supercapacitor with Ultrahigh Scan Rate Operability of 250 000 MV/s by Thermal Engineering of the Electrode-Electrolyte Interface. *ACS Appl. Energy Mater.* **2020**, *3*, 3454−3464.

(39) Rathi, P.; Jha, M. K.; Hata, K.; Subramaniam, C. Real-Time, Wearable, Biomechanical Movement Capture of Both Humans and Robots with Metal-Free Electrodes. *ACS Omega* **2017**, *2*, 4132−4142.

(40) Kobashi, K.; Ata, S.; Yamada, T.; Futaba, D. N.; Yumura, M.; Hata, K. A Dispersion Strategy: Dendritic Carbon Nanotube Network Dispersion for Advanced Composites. *Chem. Sci.* **2013**, *4*, 727−733.

(41) Modi, A.; Koratkar, N.; Lass, E.; Wei, B.; Ajayan, P. M. Miniaturized Gas Ionization Sensors Using Carbon Nanotubes. *Nature* **2003**, *424*, 171−174.
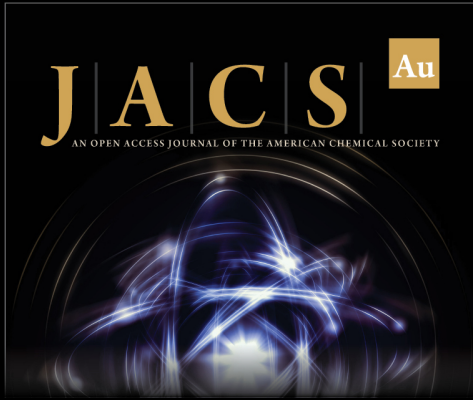
(42) Gajarushi, A. S.; Wasim, M.; Nabi, R.; Kancharlapalli, S.; Rao, V. R.; Rajaraman, G.; Subramaniam, C.; Shanmugam, M. Lanthanide Complexes as Molecular Dopants for Realizing Air-Stable n-Type Graphene Logic Inverters with Symmetric Transconductance. *Mater. Horiz.* **2019**, *6*, 743−750.

(43) Zettl, A. Extreme Oxygen Sensitivity of Electronic Properties of Carbon Nanotubes. *Science* **2000**, *287*, 1801−1804.

(44) Rose, R. A.; Orr-Ewing, A. J.; Yang, C. H.; Vidma, K.; Groenenboom, G. C.; Parker, D. H. Photodissociation Dynamics of the A $2\Sigma+$ State of SH and SD Radicals. *J. Chem. Phys.* **2009**, *130*, 034307−034314.

(45) Chase, M. W. NIST-JANAF Thermochemical Tables, 4th Ed. J. Phys. Chem. Ref. Data. 1998, Monograph 9(Part I and Part II). *J. Phys. Chem. Ref. Data.* **1998**, p Part I&II.

(46) Jung, H. Y.; Kim, Y. L.; Park, S.; Datar, A.; Lee, H.; Huang, J.; Somu, S.; Busnaina, A.; Jung, Y. J.; Kwon, Y.-K. High performance H_2S detection by redox reactions in semiconducting carbon nanotube-based device. *Analyst* **2013**, *138*, 7206−7211.